

# A MAP-Based Algorithm for Destriping and Inpainting of Remotely Sensed Images

Huanfeng Shen and Liangpei Zhang, *Member, IEEE*

**Abstract**—Remotely sensed images often suffer from the common problems of stripe noise and random dead pixels. The techniques to recover a good image from the contaminated one are called image destriping (for stripes) and image inpainting (for dead pixels). This paper presents a maximum *a posteriori* (MAP)-based algorithm for both destriping and inpainting problems. The main advantage of this algorithm is that it can constrain the solution space according to *a priori* knowledge during the destriping and inpainting processes. In the MAP framework, the likelihood probability density function (PDF) is constructed based on a linear image observation model, and a robust Huber–Markov model is used as the prior PDF. The gradient descent optimization method is employed to produce the desired image. The proposed algorithm has been tested using moderate resolution imaging spectrometer images for destriping and China–Brazil Earth Resource Satellite and QuickBird images for simulated inpainting. The experiment results and quantitative analyses verify the efficacy of this algorithm.

**Index Terms**—Destriping, inpainting, maximum *a posteriori* (MAP), remotely sensed image.

## I. INTRODUCTION

IN A LARGE number of spaceborne and airborne multideck spectrometer images, the so-called bad pixels commonly exist. Bad pixels are pixels that either do not respond electrically or have a behavior that is statistically different from surrounding pixels. The causes of the bad pixels include nonresponse of detector, relative gain and/or offset variations of detectors, calibration errors, and so on. Generally, bad pixels can be classified into warm and dead pixels. Warm pixels are those pixels which are, to some extent, brighter or darker than the healthy pixels. Dead pixels are those pixels whose measurement does not have any correlation with the true scene that is being measured [1]. Since linear charge-coupled devices are commonly employed, the bad pixels are often linearly distributed in the image in strips. Furthermore, the existence

of randomly distributed dead pixels is also possible. These severely degrade the quality of the imagery. The correction of image stripes is commonly called image destriping. The recovery of the dead pixels sometimes goes by the name of dead pixel replacement. In this paper, however, another more attractive name is used, i.e., image inpainting, which has been widely used in the field of digital image processing [2]–[4].

The simplest destriping technique is to process the image data with a low-pass filter in the frequency domain using the discrete Fourier transform. This method has the advantage of being usable on georectified images, but it often does not remove all stripes and leads to significant blurring within the image. Some researchers remove the stripes using wavelet analysis, which takes advantage of the scaling and directional properties to detect and eliminate striping patterns [5], [6]. However, the blurring problem also exists in this type of method [7]. To overcome the disadvantage of the conventional filtering-based methods, Chen *et al.* [8] proposed a method to distinguish the striping-induced frequency components using the power spectrum, and then, the stripes are removed using a power finite-impulse response filter.

Another destriping approach examines the distribution of digital numbers (DNs) for each sensor and adjusts this distribution to some reference distribution [7], [9]. Obviously, this approach assumes similarity of the data. Algazi and Ford [10] use the equalization method for destriping National Oceanic and Atmospheric Administration (NOAA)-3 and NOAA-4 satellite data. Corsini *et al.* [11] remove the stripes in MOS-B data by estimating the equalization curve on homogeneous targets. Gadallah *et al.* [9] use a moment matching method to remove the stripes in Landsat thematic mapper (TM) remote sensing images. Liu *et al.* [12] eliminate the horizontal and vertical striping patterns in enhanced TM imageodesy images by semiautomatic fast Fourier transform selective and adaptive filtering procedures. Horn and Woodham [13] and Wegener [14] discussed histogram matching for destriping problems. More recently, Rakwatin *et al.* [7] combined histogram matching with a facet filter for stripe noise reduction (NR) in moderate resolution imaging spectrometer (MODIS) data.

For the inpainting problem, the nearest neighbor, average, or median value replacement methods are commonly employed [1]. The main disadvantage of these methods is that they are employable only when the dead area is small (for example, the width of the dead line is only one or two pixels). Even for dead areas just a little larger, these methods will produce obvious artifacts. Wang *et al.* [15] provide a method to retrieve Aqua MODIS band 6 using other bands based on their relationships in Terra MODIS.

Manuscript received January 29, 2008; revised May 4, 2008 and June 24, 2008. First published December 9, 2008; current version published April 24, 2009. This work was supported in part by the Major State Basic Research Development Program 2009CB723905, by the 863 Program of the People's Republic of China under Grant 2007AA12Z148, by the National Natural Science Foundation of China under Grants 40771139 and 40801182, and by the Foundation of Key Laboratory of Resource Remote Sensing and Digital Agriculture under Grant RDA0801.

H. Shen is with the School of Resource and Environmental Science, and State Key Laboratory of Information Engineering in Surveying, Mapping, and Remote Sensing, Wuhan University, Wuhan 430079, China (e-mail: shenhf@whu.edu.cn).

L. Zhang is with the State Key Laboratory of Information Engineering in Surveying, Mapping, and Remote Sensing, Wuhan University, Wuhan 430079, China (e-mail: zlp62@public.wh.hb.cn).

Color versions of one or more of the figures in this paper are available online at <http://ieeexplore.ieee.org>.

Digital Object Identifier 10.1109/TGRS.2008.2005780

It is worth noting that both destriping and inpainting are ill-posed inverse problems because it is necessary to the recovery of a high-quality image from a degraded image. The problem is typically that a multiplicity of possible solutions exists. The accepted approach to tackling such problems is to constrain the solution space according to *a priori* knowledge on the form of the solution [16]. To our knowledge, few publications include the prior (or regularization) constraint for destriping or inpainting of remotely sensed images. In this paper, a maximum *a posteriori* (MAP)-based algorithm is proposed for both destriping and inpainting problems. This algorithm can effectively make use of the neighbor *a priori* constraint of the image and produces the desired results.

The remainder of this paper is organized as follows. In Section II, the image observation model and the MAP-based recovery model are formulated. The optimization method is presented in Section III. In Section IV, the parameter determination methods are described. Experimental results are provided in Section V, and Section VI concludes this paper.

## II. PROBLEM FORMULATION

### A. Image Observation Model

The first step to comprehensively analyze the destriping and inpainting problems is to assume an image observation model with which we can relate the desired image to the degraded image. Letting  $z_{x,y}$  and  $g_{x,y}$  denote the input radiance to be measured and the sensor output of location  $(x, y)$ , respectively, the relationship between  $z_{x,y}$  and  $g_{x,y}$  is of the form

$$g_{x,y} = f_{x,y}(z_{x,y}) \quad (1)$$

where  $f_{x,y}$  is a linear or nonlinear function. For regular image stripes, the function  $f_{x,y}$  is commonly assumed to be only dependent on the line index [17]. However, in order to include random dead pixels in the model, it will still be denoted on the pixel-by-pixel basis, as shown in (1). In this paper, it is assumed that the degradation process can be linearly described as in [9] and [17], but the existence of linear-assumption error is permitted. Thus, (1) can be rewritten as

$$g_{x,y} = A_{x,y}z_{x,y} + B_{x,y} + n_{x,y} \quad (2)$$

where  $A_{x,y}$  and  $B_{x,y}$  are the relative gain and offset parameters, respectively, and  $n_{x,y}$  is the sum of linear-assumption error and sensor noise. In matrix-vector form, the relation between the observed image and the desired image can be expressed as

$$\mathbf{g} = \mathbf{A}\mathbf{z} + \mathbf{B} + \mathbf{n}. \quad (3)$$

In the model,  $\mathbf{g}$  is the lexicographically ordered vector of the observed image,  $\mathbf{z}$  represents the desired image,  $\mathbf{A}$  is a diagonal matrix with diagonal elements being the gains of all pixels,  $\mathbf{B}$  is the offset vector, and  $\mathbf{n}$  represents the noise vector.

### B. Map-Based Recovery Model

In recent years, the MAP estimation method, which inherently includes *a priori* constraints in the form of prior

probability density functions (PDFs), has enjoyed increasing popularity. It has been central to the solution of ill-posed inverse problems in a wide range of applications [16], such as image denoising [18], deblurring [19], super resolution reconstruction [20], and others. Inspired by these, an attempt was made to use the MAP framework for the destriping and inpainting problems of remotely sensed images. The purpose is to realize the MAP estimate of a destriped or inpainted image  $\mathbf{z}$ , given the degraded image  $\mathbf{g}$ . It can be computed by

$$\hat{\mathbf{z}} = \arg \max_{\mathbf{z}} p(\mathbf{z}|\mathbf{g}). \quad (4)$$

Applying Bayes' rule, (4) becomes

$$\hat{\mathbf{z}} = \arg \max_{\mathbf{z}} \frac{p(\mathbf{g}|\mathbf{z})p(\mathbf{z})}{p(\mathbf{g})}. \quad (5)$$

Since  $p(\mathbf{z}|\mathbf{g})$  is independent of  $\mathbf{g}$ ,  $p(\mathbf{g})$  can be considered a constant, and hence, (5) can be rewritten as

$$\hat{\mathbf{z}} = \arg \max_{\mathbf{z}} p(\mathbf{g}|\mathbf{z})p(\mathbf{z}). \quad (6)$$

Using the monotonic logarithm function, (6) can be expressed as

$$\hat{\mathbf{z}} = \arg \max_{\mathbf{z}} \{\log p(\mathbf{g}|\mathbf{z}) + \log p(\mathbf{z})\}. \quad (7)$$

It is seen that two PDFs need to be constructed. The first is the likelihood density function, which provides a measure of the conformance of the estimated image to the observed image according to the image observation model. It is determined by the probability density of the noise vector in (3), i.e.,  $p(\mathbf{g}|\mathbf{z}) = p(\mathbf{n})$ . The zero mean Gaussian independent and identically distributed (IID) noise is often assumed. However, the IID assumption is not appropriate for the destriping and inpainting problems because different pixels may be degraded to different degrees (they may be healthy, warm, or dead). With this in mind, the noise is assumed not to be identical but still independent. Under these assumptions, the probability density is given by

$$p(\mathbf{g}|\mathbf{z}) = \frac{1}{M_1} \exp \left\{ -\frac{1}{2} (\mathbf{g} - \mathbf{A}\mathbf{z} - \mathbf{B})^T \mathbf{K}^{-1} (\mathbf{g} - \mathbf{A}\mathbf{z} - \mathbf{B}) \right\} \quad (8)$$

where  $M_1$  is a constant, and  $\mathbf{K}$  is the covariance matrix that describes the noise. Since the noise is assumed to be independent,  $\mathbf{K}$  is a diagonal matrix containing the noise variances. Rewriting (8) gives

$$p(\mathbf{g}|\mathbf{z}) = \frac{1}{M_1} \exp \left\{ -\frac{1}{2} \|\mathbf{Q}(\mathbf{g} - \mathbf{A}\mathbf{z} - \mathbf{B})\|^2 \right\}. \quad (9)$$

In this expression,  $\mathbf{Q}$  is also a diagonal matrix with

$$q_{ii} = (k_{ii})^{-1/2}. \quad (10)$$

Here,  $q_{ii}$  and  $k_{ii}$  are the diagonal elements of  $\mathbf{Q}$  and  $\mathbf{K}$ , respectively.

The second density function in (7) is the image prior, which imposes the spatial constraints on the image. This may

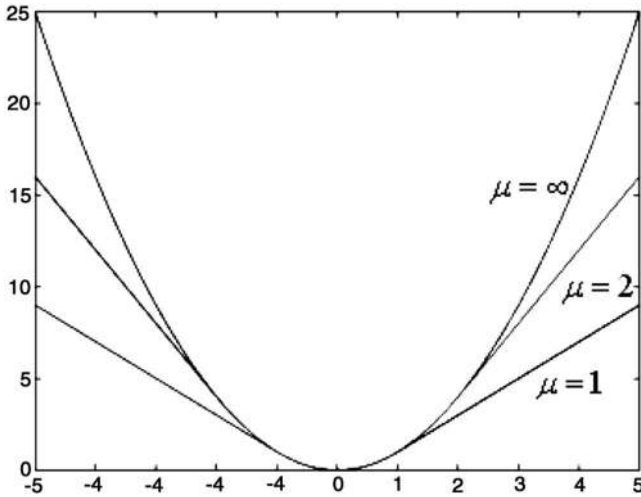


Fig. 1. Huber function with different  $\mu$ 's.

include such constraints such as positivity, smoothness, and so on. Some conventional models such as Laplacian prior and Gauss–Markov prior regularize the corresponding ill-posed problem by forcing spatial smoothness on the image. For example, the general form of the Markov prior is denoted by

$$p(\mathbf{z}) = \frac{1}{M_2} \exp \left( -\frac{1}{2\lambda} \sum_{x,y} \sum_{c \in C} \rho(d_c(z_{x,y})) \right). \quad (11)$$

In this expression,  $M_2$  is a constant,  $c$  is a clique within the set of all image cliques  $C$ , and the quantity  $d_c(z_{x,y})$  is a spatial activity measure to pixel  $z_{x,y}$ , which is often formed by first- or second-order differences. When  $\rho(\cdot)$  is a quadratic potential function as in (12), the corresponding prior is regarded as Gauss–Markov

$$\rho(i) = i^2. \quad (12)$$

The criticism of the use of the Gauss–Markov prior (and the Laplacian prior) is that some high-frequency energy in the image tends to be removed. Therefore, an edge-preserving Huber–Markov image prior is employed in this paper. This prior can effectively preserve the edge and detailed information in the image [21], [22]. The difference between the Huber–Markov prior and the Gauss–Markov prior is only the potential function  $\rho(\cdot)$ . The Huber function is defined as

$$\rho(i) = \begin{cases} i^2, & |i| \leq \mu \\ 2\mu|i| - \mu^2, & |i| > \mu \end{cases} \quad (13)$$

where  $\mu$  is a threshold parameter separating the quadratic and linear regions [21], as shown in Fig. 1. It is easy to see that the Gauss–Markov prior can be regarded as a special case of the Huber–Markov prior when  $\mu$  approaches  $+\infty$ .

As for the  $d_c(z_{x,y})$ , the following finite second-order differences are computed in four adjacent cliques for every location  $(x, y)$  in the image:

$$d_c^1(z_{x,y}) = z_{x-1,y} - 2z_{x,y} + z_{x+1,y} \quad (14)$$

$$d_c^2(z_{x,y}) = z_{x,y-1} - 2z_{x,y} + z_{x,y+1} \quad (15)$$

$$d_c^3(z_{x,y}) = \frac{1}{\sqrt{2}} [z_{x-1,y-1} - 2z_{x,y} + z_{x+1,y+1}] \quad (16)$$

$$d_c^4(z_{x,y}) = \frac{1}{\sqrt{2}} [z_{x-1,y+1} - 2z_{x,y} + z_{x+1,y-1}]. \quad (17)$$

Substituting (9) and (11) in (7), after some manipulation,  $M_1$  and  $M_2$  can be safely dropped, and the maximization of this posterior probability distribution is equivalent to the following regularized minimum problem [20]:

$$\hat{\mathbf{z}} = \arg \min [E(\mathbf{z})] \quad (18)$$

where

$$E(\mathbf{z}) = \lambda \|\mathbf{Q}(\mathbf{g} - \mathbf{A}\mathbf{z} - \mathbf{B})\|^2 + \sum_{x,y} \sum_{c \in C} \rho(d_c(z_{x,y})) \quad (19)$$

is the cost function in which the first term  $\|\mathbf{Q}(\mathbf{g} - \mathbf{A}\mathbf{z} - \mathbf{B})\|^2$  is the data fidelity term and  $\sum_{x,y} \sum_{c \in C} \rho(d_c(z_{x,y}))$  acts as the regularization term. The two competing terms correspond to the energy of PDF (9) and prior function (11), respectively. These are balanced by  $\lambda$ , which can now be called the regularization parameter.

### III. OPTIMIZATION METHOD

The gradient descent optimization method is used for the minimum problem in (18). Differentiating  $E(\mathbf{z})$  with respect to  $\mathbf{z}$  gives

$$\nabla E(\mathbf{z}) = -2\lambda \mathbf{A}^T \mathbf{Q}^T \mathbf{Q}(\mathbf{g} - \mathbf{A}\mathbf{z} - \mathbf{B}) + 2\mathbf{D}^T \rho'(\mathbf{D}\mathbf{z}) \quad (20)$$

where  $\mathbf{D}\mathbf{z}$  is a vector comprising all elements of clique set  $C$  with  $\mathbf{D}$  being the corresponding large sparse matrix. The corresponding gradient element of the prior term is given by

$$\rho'(i) = \begin{cases} 2i, & |i| \leq \mu \\ 2\mu \operatorname{sign}(i), & |i| > \mu. \end{cases} \quad (21)$$

Then, the desired image is solved by employing the successive approximations iteration

$$\hat{\mathbf{z}}_{n+1} = \hat{\mathbf{z}}_n - \beta_n \nabla E(\mathbf{z}_n) \quad (22)$$

where  $n$  is the iteration number, and  $\beta_n$  is the step size. If  $\beta_n$  is too small, the convergence will be very slow. On the other hand, if it is too large, the algorithm will be unstable or divergent. By making a second-order Taylor series approximation to the objective function at the current state  $\hat{\mathbf{z}}_n$ , a quadratic step size approximation becomes [21]

$$\beta_n = \frac{(\nabla E(\mathbf{z}_n))^T \nabla E(\mathbf{z}_n)}{(\nabla E(\mathbf{z}_n))^T (\nabla^2 E(\mathbf{z}_n)) \nabla E(\mathbf{z}_n)} \quad (23)$$

where  $\nabla^2 E(\mathbf{z})$  is the Hessian matrix of the cost function  $E(\mathbf{z})$ . The iteration is terminated when

$$\|\mathbf{z}_{n+1} - \mathbf{z}_n\|^2 / \|\mathbf{z}_n\|^2 \leq d \quad (24)$$

where  $d$  is a predetermined coefficient.

It is worth noting that (21) can be performed only on bad pixels to retain the original brightness of healthy pixels. However, if the original image was contaminated by random noise, the proposed algorithm can also be used for denoising by performing (22) on all pixels. Furthermore, it is not necessary to construct the big matrices  $\mathbf{A}$  and  $\mathbf{Q}$  and their corresponding transposes during the solution process. Since they are diagonal, the matrix-vector multiplication operations can be substituted by scalar multiplications pixel by pixel.

#### IV. PARAMETER DETERMINATION

In order to use the observation model (3),  $\mathbf{A}$  (gains) and  $\mathbf{B}$  (biases) should first be determined. It is easily understood that, for healthy pixels, the gain and bias should be one and zero, respectively. For dead pixels in image inpainting, the gain can be regarded as zero and the bias as the pixel value. For the destriping problem, the parameters of pixels in a row or a column are often assumed to be the same. Any linear adjustment method can be used to obtain the gains and biases of the stripe pixels. In this paper, the moment matching method is used [9]. Given a reference row (column), the gain and bias of the striped row (column) can be solved by

$$A = \frac{\sigma_s}{\sigma_r} \quad (25)$$

$$B = \mu_s - \mu_r \frac{\sigma_s}{\sigma_r} \quad (26)$$

where  $\mu_s$  and  $\sigma_s$  are the mean and standard deviation, respectively, of the striped row (column), and  $\mu_r$  and  $\sigma_r$  are the mean and standard deviation, respectively, of the reference row (column). It can now be seen that the moment matching method is a special case of the proposed algorithm with  $\lambda \rightarrow \infty$  and  $\mathbf{Q}$  being a unit matrix in (19).

The regularization parameter  $\lambda$  balances the data fidelity (the first term) and the image regularization (the second term). Some approaches [23], [24] have been developed to determine this parameter automatically. However, the universal applicability of these approaches for different types of images and regularization problems has not been effectively validated. Therefore, this parameter is determined heuristically in this paper.

It has been mentioned that matrix  $\mathbf{Q}$  is diagonal, and its elements represent the reciprocals of the noise standard deviation in different pixel locations [see (10)]. For convenience, the element values are scaled to the range of zero to one. The difference caused by the scaling can be balanced by  $\lambda$ . Thus, the function of  $\mathbf{Q}$  can be regarded as the relative adjustment of regularization at each pixel location. For all the healthy pixels, the corresponding elements are set to the maximum value of one. On the contrary, the elements should be zero for dead pixels because they do not have any correlation with the true scene. The elements of warm pixels are between zero and one, and they correlate with the local activity level, the validity of moment matching, and so on. Using the moment matching method, the stripes in smooth regions are often not perfectly removed. Therefore, small element values can be selected to recover the information from the neighbors using the prior constraint. On the other hand, larger element values should be

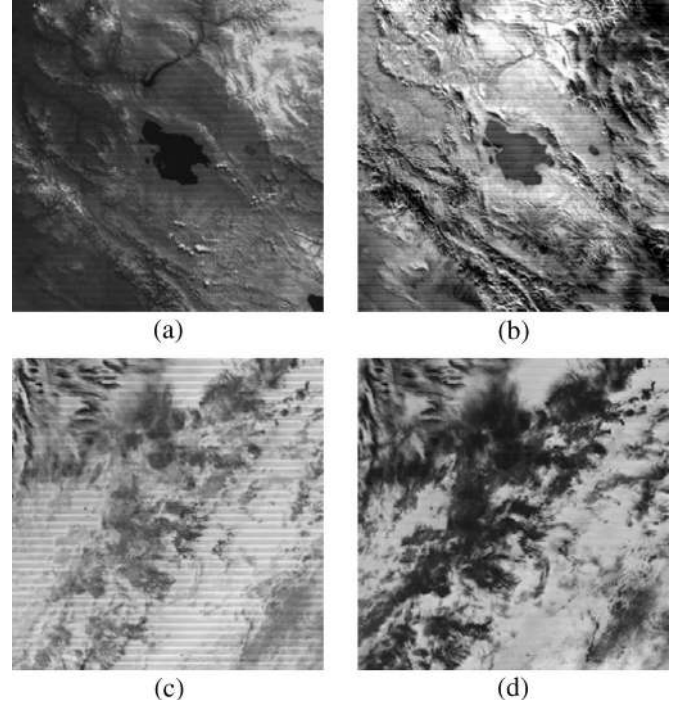


Fig. 2. MODIS subimages before destriping. (a) Aqua MODIS band 26. (b) Aqua MODIS band 30. (c) Terra MODIS band 28. (d) Terra MODIS band 30.

chosen for sharp regions in order to retain the high-frequency information. In this paper, the standard deviation is used as the activity measure, and the following equation determines the diagonal elements in  $\mathbf{Q}$ :

$$q_{ii} = \ln \left[ \frac{(e - 1)(\text{std} - \min)}{\max - \min} + 1 \right]. \quad (27)$$

In this equation, std represents the standard deviation, max and min are the std thresholds corresponding to the maximum value of one and the minimum value of zero, respectively. It is noted that the std value should be computed on a neighbor region that does not contain any stripes or dead pixels.

#### V. EXPERIMENTS

##### A. Destriping Experiments

The proposed algorithm was tested for destriping on images of the MODIS aboard the Terra and Aqua platforms. The experimental results of bands 28 and 30 of Terra MODIS data and bands 26 and 30 of Aqua MODIS data are presented in this paper. The Aqua MODIS data used in this paper were acquired on December 28, 2003, and the Terra MODIS data were acquired on September 24, 2007. Sections of size  $400 \times 400$  were extracted from the original images as experimental data. These subimages are shown in Fig. 2(a)–(d). For calculation and display convenience, the original data are coded to an 8-B scale.

In order to show that the proposed algorithm is not very sensitive to the parameter set, the same parameters were used in the four series of destriping experiments, i.e.,  $\lambda = 15$ ,  $\mu = 5$ ,  $\min = 3$ ,  $\max = 255$ , and  $d = 1 \times 10^{-6}$ . The Butterworth low-pass filtering, moment matching, and histogram matching

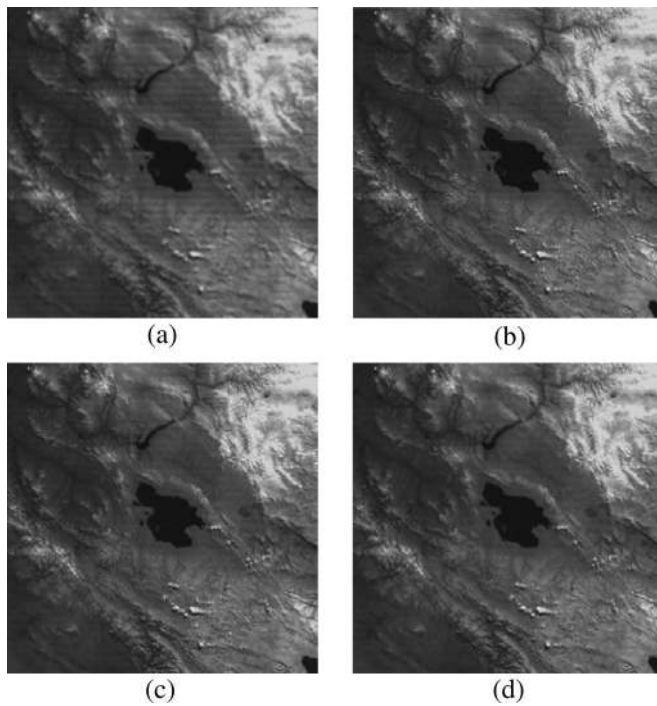


Fig. 3. Destriped results of Aqua MODIS band 26. (a) Butterworth filtering. (b) Moment matching. (c) Histogram matching. (d) Proposed algorithm.

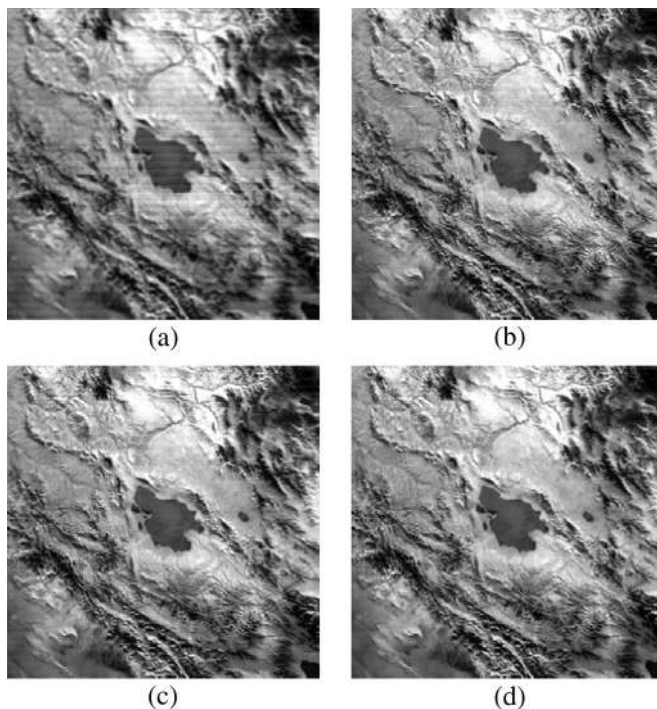


Fig. 4. Destriped results of Aqua MODIS band 30. (a) Butterworth filtering. (b) Moment matching. (c) Histogram matching. (d) Proposed algorithm.

destriping methods were also tested to make a comparative analysis with the proposed algorithm. Experimental results of the four test images are shown in Figs. 3–6. It can be seen that Butterworth filtering does not remove all stripes in the image and leads to significant blurring. Moment matching and histogram matching can greatly improve the image quality, but there are still considerable radiance fluctuations within the

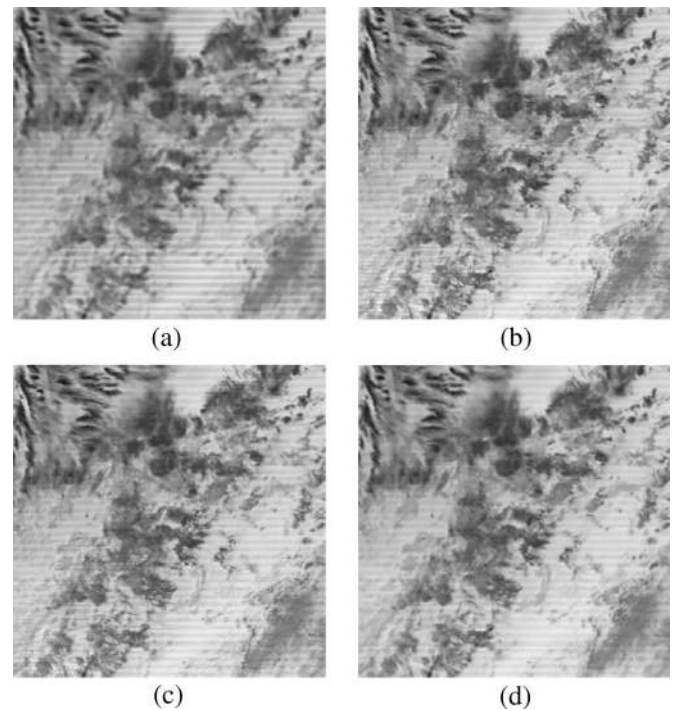


Fig. 5. Destriped results of Terra MODIS band 28. (a) Butterworth filtering. (b) Moment matching. (c) Histogram matching. (d) Proposed algorithm.

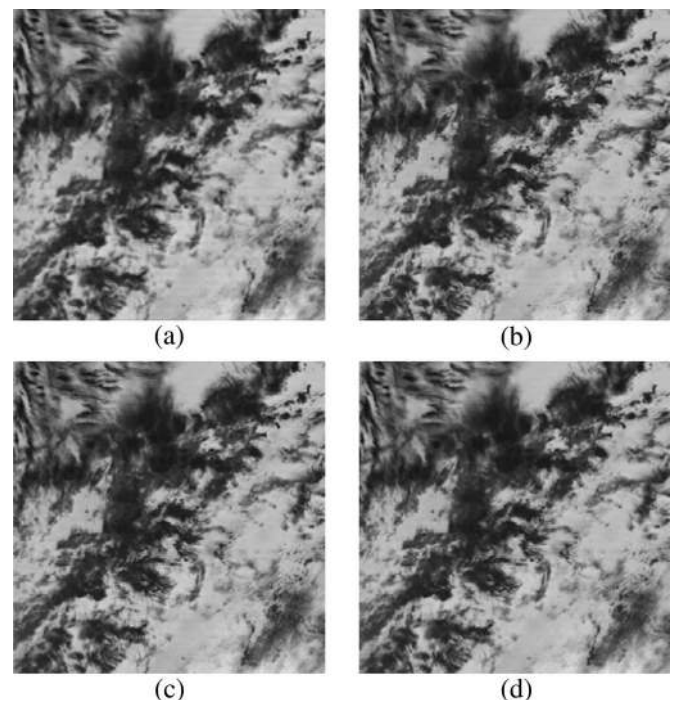


Fig. 6. Destriped results of Terra MODIS band 30. (a) Butterworth filtering. (b) Moment matching. (c) Histogram matching. (d) Proposed algorithm.

resulting image. The proposed algorithm, however, provides a much more robust destriping from the visual perspective.

Fig. 7 shows the mean cross-track profiles of the original test images. The horizontal axis represents the line number, and the vertical axis represents the mean DN of each line. Due to the existence of stripes, there are rapid fluctuations at constant frequency in the curves. Fig. 8 shows the profiles of

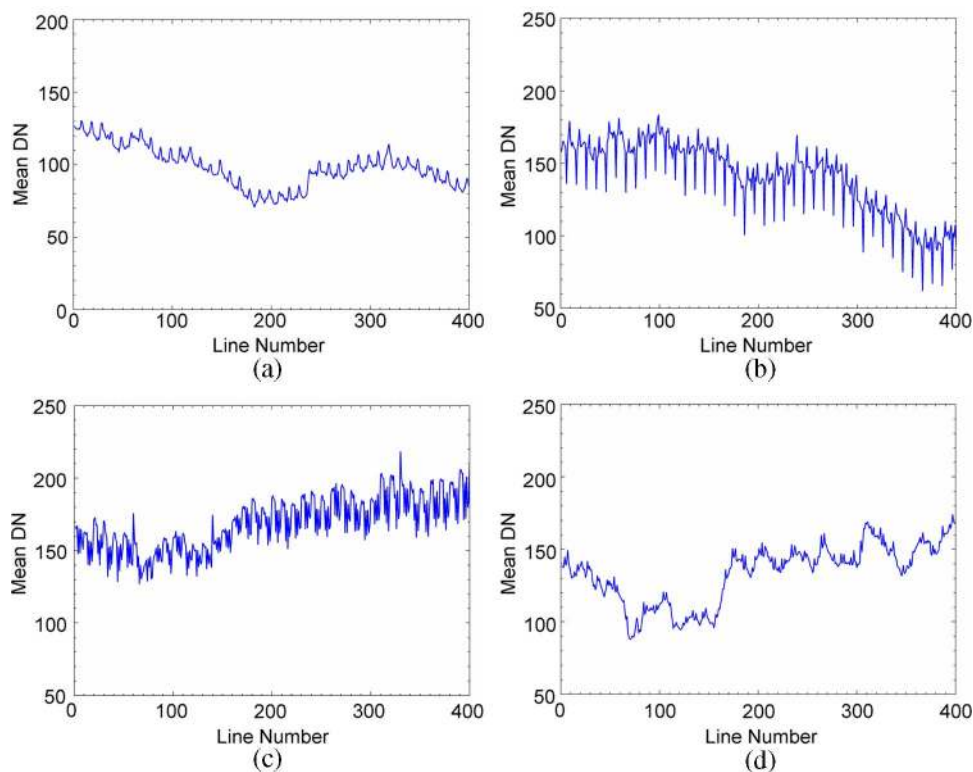


Fig. 7. Mean cross-track profiles of MODIS images before destriping. (a) Aqua MODIS band 26. (b) Aqua MODIS band 30. (c) Terra MODIS band 28. (d) Terra MODIS band 30.

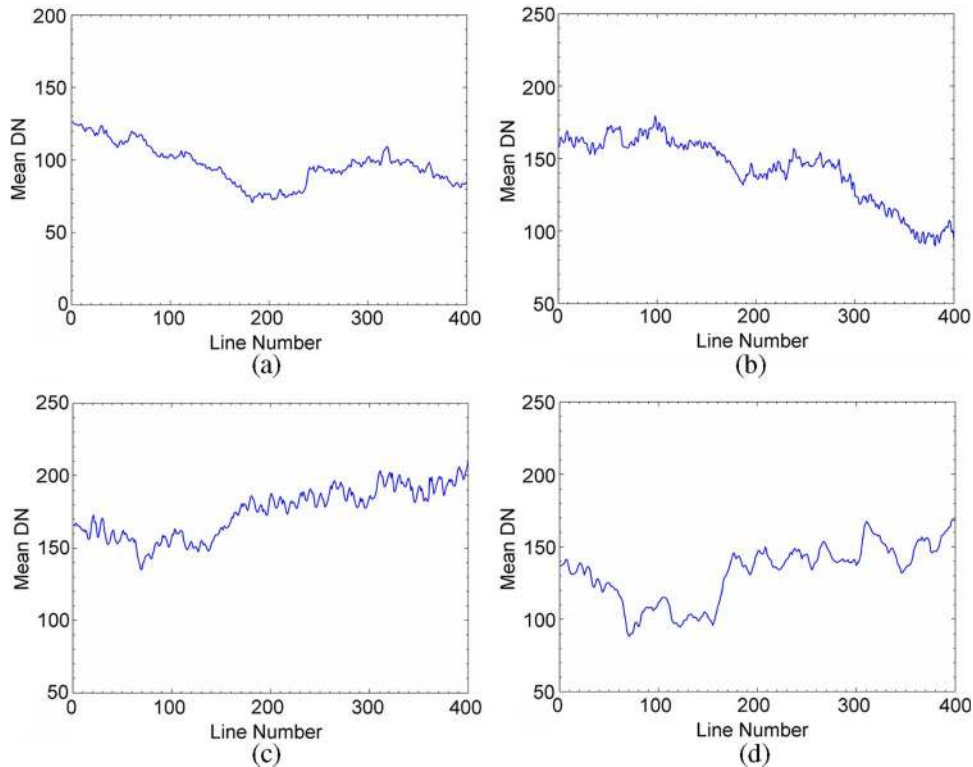


Fig. 8. Mean cross-track profiles of the destriped MODIS images using the proposed algorithm. (a) Aqua MODIS band 26. (b) Aqua MODIS band 30. (c) Terra MODIS band 28. (d) Terra MODIS band 30.

destriped images processed by the proposed algorithm. It can be seen that the fluctuations are very much reduced. Figs. 9 and 10 show the Fourier transforms of the test images and

the destriped images of the proposed algorithm. The horizontal axis represents the normalized frequency, and the vertical axis represents the averaged power spectrum of all columns. For



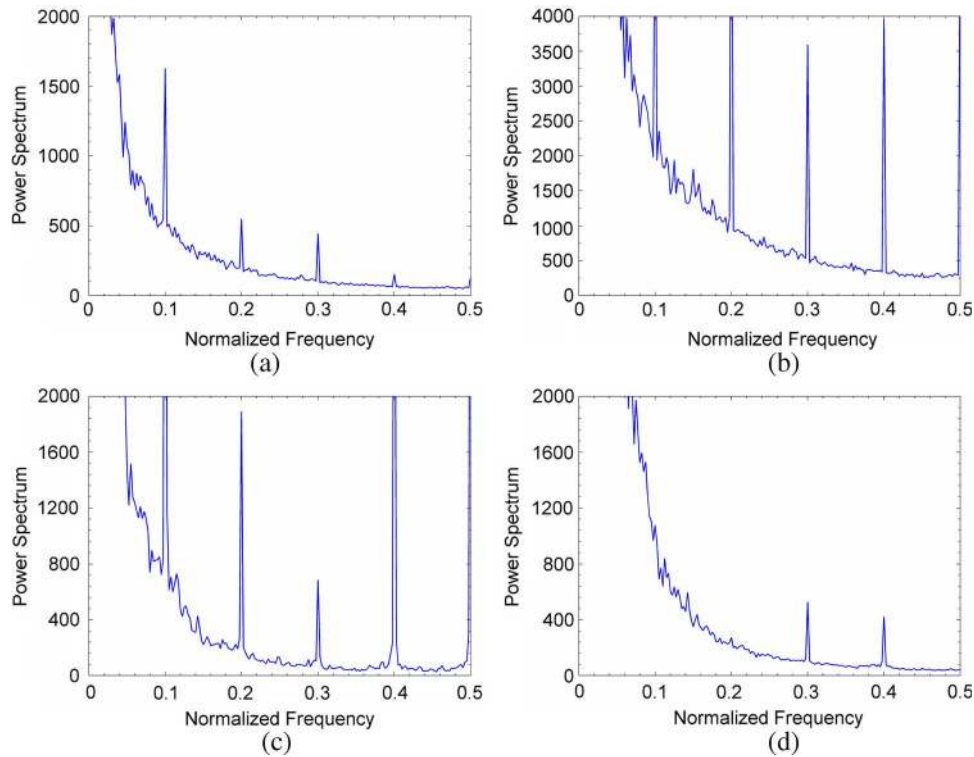


Fig. 9. Mean column power spectrum of the MODIS images before destriping. (a) Aqua MODIS band 26. (b) Aqua MODIS band 30. (c) Terra MODIS band 28. (d) Terra MODIS band 30.

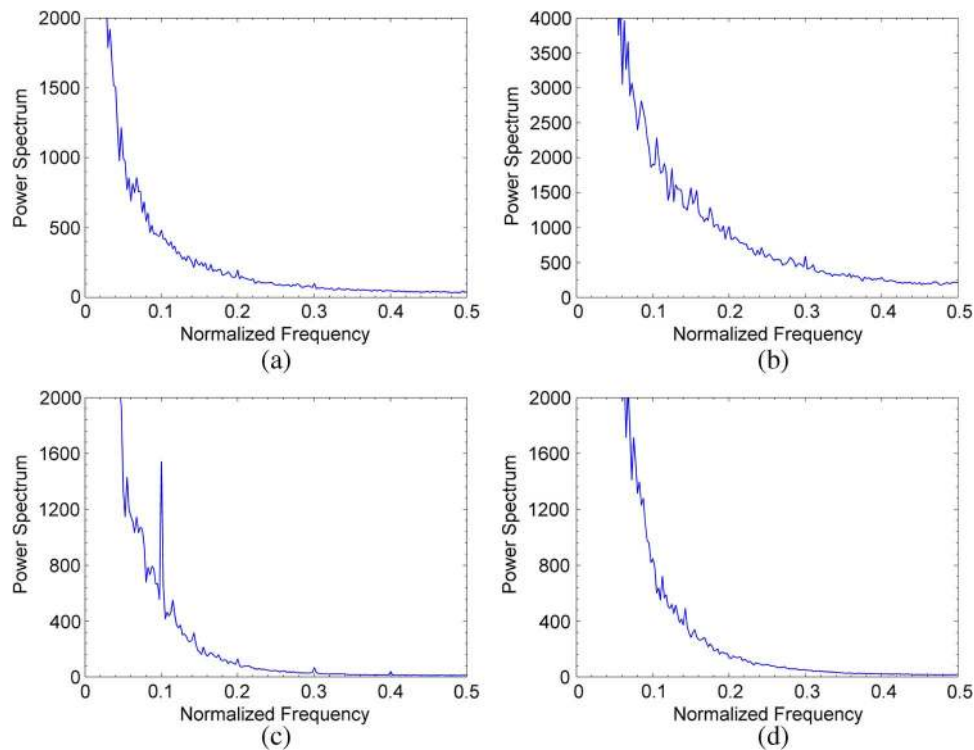


Fig. 10. Mean column power spectrum of the destriped MODIS images using the proposed algorithm. (a) Aqua MODIS band 26. (b) Aqua MODIS band 30. (c) Terra MODIS band 28. (d) Terra MODIS band 30.

better visualization of NR, very high spectral magnitudes are not plotted. Since the MODIS sensor has ten detectors, the pulses caused by (detector-to-detector) stripes are located at the frequencies of  $1/10$ ,  $2/10$ ,  $3/10$ ,  $4/10$ , and  $5/10$  cycles (see Fig. 9).

In Fig. 10, it is easily recognized that the value of the power spectrum of the frequency components where the pulses exist has been strongly reduced. Fig. 11 shows the power spectrum of the destriped results of Fig. 11(b) using the Butterworth

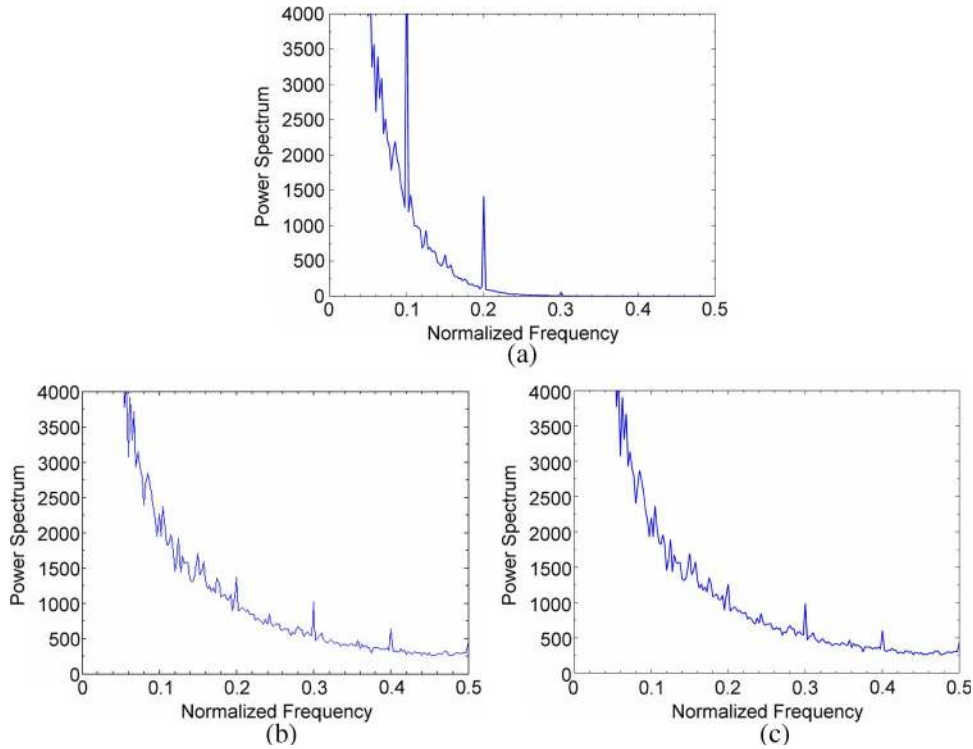


Fig. 11. Mean column power spectrum of the destriped images (Aqua MODIS band 30) using (a) Butterworth filtering, (b) moment matching, and (c) histogram matching.

TABLE I  
ICVs AND MRDs OF THE ORIGINAL AND DESTRIPIED MODIS DATA

		Original	Butterworth	Moment	Histogram	Proposed
Aqua Band 26	Sample1 (ICV)	17.04	22.08	27.95	31.36	36.27
	Sample2 (ICV)	16.41	23.86	30.50	27.56	35.48
	Sample3 (MRD)	0.0%	14.5%	0.0%	0.0%	0.0%
Aqua Band 30	Sample1 (ICV)	7.94	14.49	24.42	22.72	27.36
	Sample2 (ICV)	9.66	15.74	21.03	24.86	30.52
	Sample3 (MRD)	0.0%	62.8%	0.0%	0.0%	0.0%
Terra Band 28	Sample1 (ICV)	12.11	21.10	25.72	27.47	32.99
	Sample2 (ICV)	14.55	22.78	33.99	36.34	46.98
	Sample3 (MRD)	0.0%	8.8%	0.0%	0.0%	0.0%
Terra Band 30	Sample1 (ICV)	60.61	134.18	61.35	70.47	177.95
	Sample2 (ICV)	51.86	86.43	77.68	74.83	87.17
	Sample3 (MRD)	0.0%	11.1%	0.0%	0.0%	0.0%

filtering, moment matching, and histogram matching. Fig. 11(a) shows that Butterworth filtering loses most high-frequency components during the destriping. Fig. 11(b) and (c) shows that moment matching and histogram matching have the ability to retain frequency components but cannot effectively remove the frequency pulse caused by stripes.

To give a quantitative measure of these images, three quality indexes are employed. These are the inverse coefficient of variation (ICV), mean relative deviation (MRD), and ratio of NR. The ICV used in [7], [25], and [26] is defined as

$$ICV = \frac{R_a}{R_{sd}} \quad (28)$$

where  $R_a$  is the signal response of a homogeneous image region and is calculated by averaging the pixels within a window of a given size, and  $R_{sd}$  refers to the noise components estimated

by calculating the standard deviation of the pixel [7]. It is easily understood that the ICV index evaluates the level of stripe noise and so would be calculated for homogeneous striped regions. On the contrary, the MRD index is used to evaluate the performance of the algorithms to retain the information of image regions that are not affected by stripes. It is calculated by

$$MRD = \frac{1}{MN} \sum_{i=1}^{MN} \frac{|\hat{z}_i - g_i|}{g_i} \times 100\% \quad (29)$$

where  $g_i$  is the pixel value of the original image,  $\hat{z}_i$  is the pixel value of the destriped image, and MN is the total number of pixels. In the experiments, two  $10 \times 10$  homogeneous regions were selected for the ICV evaluation and one sharp region with about 100 pixels for the MRD evaluation. The ICV and MRD evaluation results are shown in Table I. Since



TABLE II  
NR RATIOS OF THE ORIGINAL AND DESTRIPIED MODIS DATA

	Original	Butterworth	Moment	Histogram	Proposed
Aqua Band 26	1.00	2.12	2.36	2.61	3.35
Aqua Band 30	1.00	4.26	4.82	5.05	6.89
Terra Band 28	1.00	3.65	7.69	8.05	12.08
Terra Band 30	1.00	2.46	1.85	1.87	2.18

the moment matching, histogram matching, and the proposed algorithm do not change the brightness of healthy pixels, the corresponding MRDs are all 0.0%. The Butterworth low-pass filtering, however, corresponds to poor MRDs, which is the root of image blurring. From the ICV perspective, the proposed algorithm greatly outperforms other destriping algorithms.

The NR method [7], [8] is used to evaluate the destriped image in the frequency domain. It is defined by

$$NR = \frac{N_0}{N_1} \quad (30)$$

where  $N_0$  is the power of the frequency components produced by stripes in the original image and  $N_1$  for the destriped image.  $N_0$  and  $N_1$  can be calculated by

$$N_i = \sum_{\varphi} P_i(D) \quad (31)$$

where  $P_i(D)$  is the averaged power spectrum down the columns of an image with  $D$  being the distance from the origin in Fourier space, and  $\varphi$  is the stripe noise region of the spectrum. The NR evaluation results are shown in Table II. The proposed algorithm always obtains the highest NR value, except in the case of Terra band 30. Since the stripe noise is relatively small, Butterworth filtering obtains higher NR values than the proposed algorithm. However, it pays the price of blurring the image [see Fig. 6(a)].

### B. Inpainting Experiments

In the inpainting experiments, the first test of the algorithm was for the recovery of vertical dead lines using a China–Brazil Earth Resource Satellite (CBERS) image. Fig. 12(a) shows the original subimage. In general, the wider is the dead region, the more difficult is the inpainting. This experiment tested two simulated images, which are contaminated by dead lines of five- and eight-pixel widths. They are shown in Fig. 12(b)–(e), respectively. To make a comparative analysis, the average algorithm was implemented using the “Replace Bad Lines” function in ENVI 4.4 and the results compared with those of the proposed algorithm. Since ENVI 4.4 can only deal with horizontal dead lines, the image was first rotated through  $90^\circ$ , and then, an inverse rotation was performed on the resulting image. Fig. 12(c) and (d) are the inpainted results of Fig. 12(b) using the average and proposed algorithms, respectively. The inpainted results of Fig. 12(e) are shown in Fig. 12(f) (average algorithm) and Fig. 12(g) (the proposed algorithm). In the results using the average algorithm, strong artifacts appear

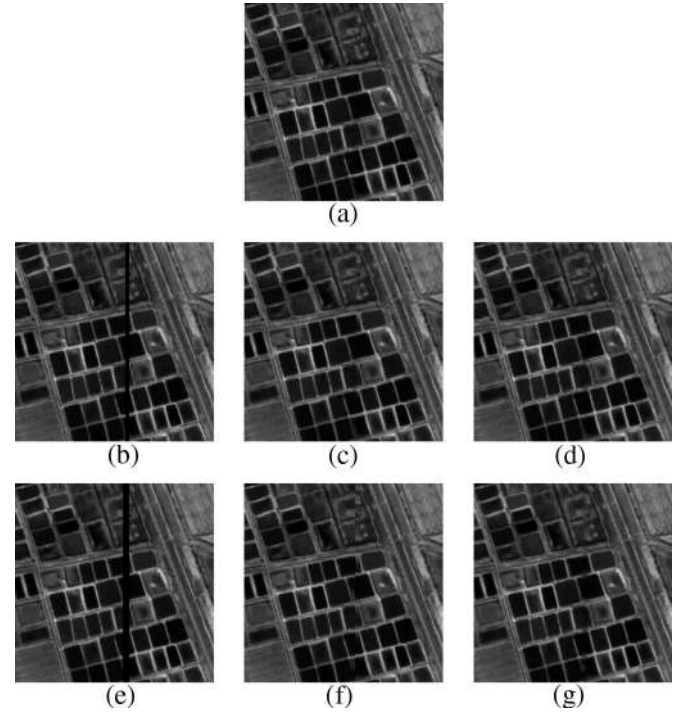


Fig. 12. Inpainting experimental results for the recovery of vertical dead lines. (a) Original image. (b) Simulated image contaminated by dead line of five-pixel width. (c) Inpainted image of (b) using the average algorithm in ENVI 4.4. (d) Inpainted image of (b) using the proposed algorithm. (e) Simulated image contaminated by dead line of eight-pixel width. (f) Inpainted image of (e) using the average algorithm in ENVI 4.4. (g) Inpainted image of (e) using the proposed algorithm.

because the dead region is relatively wide. The proposed algorithm, however, is more robust for the increase in width of the dead region. Although the lost information cannot be completely recovered, the visual quality of the results is more convincing. For the convenience of visual judgment, a series of detailed regions cropped from Fig. 12(a)–(g) are shown in Fig. 13(a)–(g). The following peak signal-to-noise ratio (PSNR) was employed as a quantitative measure:

$$PSNR = 10 \log_{10} \left( \frac{255^2 * MN}{\|\hat{z} - z\|^2} \right) \quad (32)$$

where  $MN$  is the total number of pixels in the image, and  $\hat{z}$  and  $z$  represent the inpainted and original images, respectively. The PSNRs of Fig. 12(b)–(g) are shown in Table III.

Next, the proposed algorithm was tested for another type of inpainting problem in which dead pixels are randomly distributed. Fig. 14(a) shows an original QuickBird subimage whose dimensions are  $256 \times 256$ . Fig. 14(b) shows the contaminated

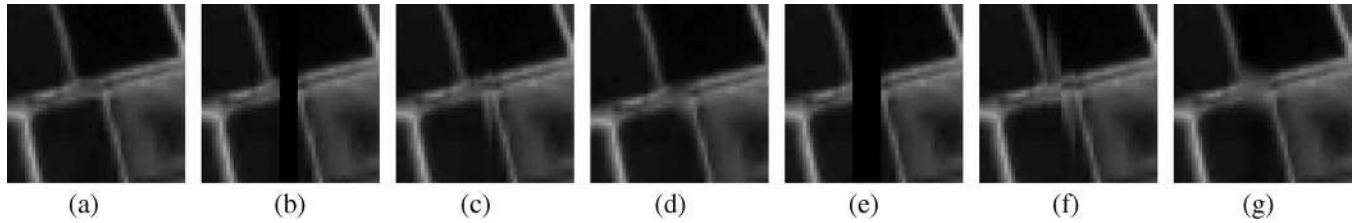


Fig. 13. (a)–(g) Detailed regions cropped from Fig. 12(a)–(g).

TABLE III  
PSNR VALUES OF THE CONTAMINATED AND INPAINTED  
CBERS DATA (IN DECIBELS)

Dead region width	Contaminated image	Average (ENVI 4.4)	Proposed algorithm
5-pixel	30.28	40.14	44.64
8-pixel	28.38	36.13	40.13

TABLE IV  
PSNR VALUES OF THE CONTAMINATED AND INPAINTED  
QUICKBIRD DATA (IN DECIBELS)

Percentage of dead pixels	Contaminated image	Proposed algorithm
50%	10.72	31.83
90%	8.17	22.98

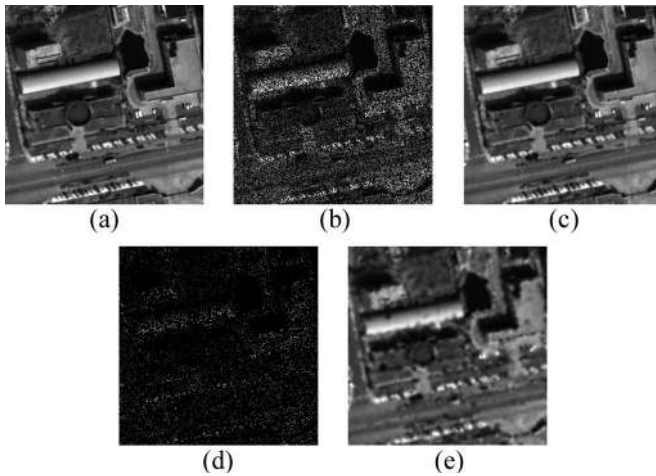


Fig. 14. Inpainting experiment for the recovery of random dead pixels. (a) Original image. (b) Image contaminated by 50% dead pixels. (c) Inpainted image of (b) using the proposed algorithm. (d) Image contaminated by 90% dead pixels. (e) Inpainted result of Fig. 14(d).

image in which the percentage of dead pixels is 50%. The inpainted image using the proposed algorithm is shown in Fig. 14(c). It is seen that most of the lost information has been recovered. In the experiment, the percentage of dead pixels was further increased to 90%. The corresponding contaminated image is shown in Fig. 14(d), in which no objects can really be seen. Fig. 14(e) shows the inpainted result of Fig. 14(d). Although the image quality is not very good because of the high percentage of dead pixels in this case, it is sufficient for the ground objects to be distinguished. The PSNR measurements are shown in Table IV. This experiment validates the strong performance of the proposed algorithm. Although such random distribution of dead pixels is not very familiar to many remote sensing users, it is often met in remote sensing preprocessing before data distribution.

## VI. CONCLUSION

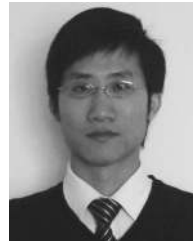
In order to constrain the solution space according to *a priori* knowledge, this paper presents a MAP-based algorithm for both destriping and inpainting problems. The proposed

algorithm was first tested on Terra and Aqua MODIS images for destriping. The image quality indexes of ICV, MRD, and ratio of NR were employed to evaluate the resulting images. Experimental results confirmed that the proposed algorithm outperforms the conventional destriping methods of low-pass filtering, moment matching, and histogram matching in terms of both the quantitative measurements and visual evaluation. However, it should be mentioned that the proposed algorithm is not easily applied to georectified data for destriping. The inpainting experiments simulated dead pixels on CBERS and QuickBird images. Experimental results indicate that the proposed algorithm is more robust than the conventional average method for wider dead regions. The proposed algorithm also has good performance when dealing with a very high percentage of random dead pixels. Nevertheless, there may still be room for the improvement of our proposed method. Using some unsymmetrical regularization models in which the knowledge that striping artifacts only exist in one direction is considered may further improve the destriping results.

## REFERENCES

- [1] B. M. Ratliff, J. S. Tyo, J. K. Boger, W. T. Black, D. L. Bowers, and M. P. Fetrow, "Dead pixel replacement in LWIR microgrid polarimeters," *Opt. Express*, vol. 15, no. 12, pp. 7596–7609, Jun. 2007.
- [2] T. F. Chan and J. Shen, "Mathematical models for local nontexture inpaintings," *SIAM J. Appl. Math.*, vol. 62, no. 3, pp. 1019–1043, 2002.
- [3] M. Bertalmio, G. Sapiro, V. Caselles, and C. Ballester, "Image inpainting," in *Proc. ACM SIGGRAPH Conf. Comput. Graph.*, New Orleans, LA, 2000, pp. 417–424.
- [4] M. Elad, J. L. Starck, P. Querre, and D. L. Donoho, "Simultaneous cartoon and texture image inpainting using morphological component analysis (MCA)," *Appl. Comput. Harmon. Anal.*, vol. 19, no. 3, pp. 340–358, Nov. 2005.
- [5] J. Torres and S. O. Infante, "Wavelet analysis for the elimination of striping noise in satellite images," *Opt. Eng.*, vol. 40, no. 7, pp. 1309–1314, Jul. 2001.
- [6] J. S. Chen, H. Lin, Y. Shao, and L. M. Yang, "Oblique striping removal in remote sensing imagery based on wavelet transform," *Int. J. Remote Sens.*, vol. 27, no. 8, pp. 1717–1723, Apr. 2006.
- [7] P. Rakwatin, W. Takeuchi, and Y. Yasuoka, "Stripe noise reduction in MODIS data by combining histogram matching with facet filter," *IEEE Trans. Geosci. Remote Sens.*, vol. 45, no. 6, pp. 1844–1856, Jun. 2007.
- [8] J. Chen, Y. Shao, H. Guo, W. Wang, and B. Zhu, "Destriping CMODIS data by power filtering," *IEEE Trans. Geosci. Remote Sens.*, vol. 41, no. 9, pp. 2119–2124, Sep. 2003.

- [9] F. L. Gadallah, F. Csillag, and E. J. M. Smith, "Destriping multisensor imagery with moment matching," *Int. J. Remote Sens.*, vol. 21, no. 12, pp. 2505–2511, Aug. 2000.
- [10] V. R. Algazi and G. E. Ford, "Radiometric equalization of nonperiodic striping in satellite data," *Comput. Graph. Image Process.*, vol. 16, no. 3, pp. 287–295, 1981.
- [11] G. Corsini, M. Diani, and T. Walzel, "Striping removal in MOS-B data," *IEEE Trans. Geosci. Remote Sens.*, vol. 38, no. 3, pp. 1439–1446, May 2000.
- [12] J. G. Liu and G. L. K. Morgan, "FFT selective and adaptive filtering for removal of systematic noise in ETM+ imageodesy images," *IEEE Trans. Geosci. Remote Sens.*, vol. 44, no. 12, pp. 3716–3724, Dec. 2006.
- [13] B. K. P. Horn and R. J. Woodham, "Destriping Landsat MSS images by histogram modification," *Comput. Graph. Image Process.*, vol. 10, no. 1, pp. 69–83, 1979.
- [14] M. Wegener, "Destriping multiple sensor imagery by improved histogram matching," *Int. J. Remote Sens.*, vol. 11, no. 5, pp. 859–875, May 1990.
- [15] L. Wang, J. J. Qu, X. Xiong, X. Hao, Y. Xie, and N. Che, "A new method for retrieving band 6 of Aqua MODIS," *IEEE Geosci. Remote Sens. Lett.*, vol. 3, no. 2, pp. 267–270, Apr. 2006.
- [16] S. Borman and R. Stevenson, "Spatial resolution enhancement of low-resolution image sequences: A comprehensive review with directions for future research," Lab. Image Signal Anal. (LISA), Univ. Notre Dame, Notre Dame, IN, Jul. 8, 1998. Report.
- [17] D. J. Poros and C. J. Peterson, "Methods for destriping Landsat thematic mapper images—A feasibility study for an online destriping process in the thematic mapper image processing system (TIPS)," *Photogramm. Eng. Remote Sens.*, vol. 51, pp. 1371–1378, 1985.
- [18] A. B. Hamza and H. Krim, "A variational approach to maximum *a posteriori* estimation for image denoising," in *Lect. Notes Comput. Sci.*, Sep. 2001, vol. 2134, pp. 19–33.
- [19] P. A. Ferrari, A. Frigessi, and P. G. de Sa, "Fast approximate maximum *a posteriori* restoration of multicolour images," *J. R. Stat. Soc., B*, vol. 57, no. 3, pp. 485–500, 1995.
- [20] H. Shen, L. Zhang, B. Huang, and P. Li, "A MAP approach for joint motion estimation, segmentation, and super resolution," *IEEE Trans. Image Process.*, vol. 16, no. 2, pp. 479–490, Feb. 2007.
- [21] R. R. Schultz and R. L. Stevenson, "Extraction of high-resolution frames from video sequences," *IEEE Trans. Image Process.*, vol. 5, no. 6, pp. 996–1011, Jun. 1996.
- [22] H. Shen, M. K. Ng, P. Li, and L. Zhang, "Super resolution reconstruction algorithm to MODIS remote sensing images," *Comput. J.*, 2007. DOI:10.1093/comjnl/bxm028. [Online]. Available: <http://comjnl.oxfordjournals.org/ogi/content/abstract/bxm028>
- [23] E. S. Lee and M. G. Kang, "Regularized adaptive high-resolution image reconstruction considering inaccurate subpixel registration," *IEEE Trans. Image Process.*, vol. 12, no. 7, pp. 826–837, Jul. 2003.
- [24] N. Nguyen, P. Milanfar, and G. Golub, "Efficient generalized cross-validation with applications to parametric image restoration and resolution enhancement," *IEEE Trans. Image Process.*, vol. 10, no. 9, pp. 1299–1308, Sep. 2001.
- [25] J. E. Nichol and V. Vohora, "Noise over water surfaces in Landsat TM images," *Int. J. Remote Sens.*, vol. 25, no. 11, pp. 2087–2093, Jun. 2004.
- [26] G. M. Smith and P. J. Curran, "Methods for estimating image signal-to-noise ratio," in *Advances in Remote Sensing and GIS Analysis*, P. M. Atkinson and N. J. Tate, Eds. Hoboken, NJ: Wiley, 2000, pp. 61–74.



**Huanfeng Shen** received the B.S. degree in surveying and mapping engineering and the Ph.D. degree in photogrammetry and remote sensing from Wuhan University, Wuhan, China, in 2002 and 2007, respectively.

In July 2007, he is with the School of Resource and Environmental Science, Wuhan University, as an Assistant Professor. His current research interests focus on image reconstruction and remote sensing image processing and application.



**Liangpei Zhang** (M'06) received the B.S. degree in physics from Hunan Normal University, Changsha, China, in 1982, the M.S. degree in optics from the Xi'an Institute of Optics and Precision Mechanics, Chinese Academy of Sciences, Xi'an, China, in 1988, and the Ph.D. degree in photogrammetry and remote sensing from Wuhan University, Wuhan, China, in 1998.

From 1997 to 2000, he was a Professor with the School of the Land Sciences, Wuhan University. In August 2000, he is with the State Key Laboratory of

Information Engineering in Surveying, Mapping and Remote Sensing, Wuhan University, as a Professor and the Head of the Remote Sensing Section. Since 2007, he has been nominated as a "ChangJiang Scholar" Professor (Chair Professor) by the Education Ministry of China. He was an Editor of the 2001 Multispectral Image Processing and Pattern Recognition (MIPPR01), MIPPR05, and Geoinformatics Symposia and an Associate Editor of the *Geospatial Information Science Journal* and the Chinese National Committee for the International Geosphere-Biosphere Program. He has published more than 150 research papers. His research interests include hyperspectral remote sensing, high resolution remote sensing, image processing, and artificial intelligence.

Dr. Zhang has served as the Cochair of the SPIE Series Conferences on MIPPR and the Conference on Asia Remote Sensing in 1999 and an executive member for China Society of Image and Graphics.